Mathematics and Computers in Simulation 229 (2025) 512–524

Contents lists available at ScienceDirect

Mathematics and Computers in Simulation

journal homepage: www.elsevier.com/locate/matcom

Original articles

Determination of emissivity profiles using a Bayesian data-driven approach

Luca Sgheri [a,*], Cristina Sgattoni [b], Chiara Zugarini [c,a]

[a] CNR-IAC, Via Madonna del Piano, 10, Sesto Fiorentino, I-50019, FI, Italy
[b] CNR-IBE, Via Madonna del Piano, 10, Sesto Fiorentino, I-50019, FI, Italy
[c] Università di Firenze, Dipartimento di Ingegneria Informatica, Via di S. Marta, 3, Firenze, I-50139, FI, Italy

ARTICLE INFO

Keywords:
FORUM
Far infrared
Emissivity retrieval
CAMEL database

ABSTRACT

In this paper, we explore the determination of a spectral emissivity profile that closely matches real data, intended for use as an initial guess and/or a priori information in a retrieval code. Our approach employs a Bayesian method that integrates the CAMEL (Combined ASTER MODIS Emissivity over Land) emissivity database with the MODIS/Terra+Aqua Yearly Land Cover Type database. The solution is derived as a convex combination of high-resolution Huang profiles using the Bayesian framework. We test our method on IASI (Infrared Atmospheric Sounding Interferometer) data and find that it outperforms the linear spline interpolation of the CAMEL data and the Huang emissivity database itself.

1. Introduction and background

Any body hit by electromagnetic radiation either absorbs or reflects the radiation. The absorbed radiation is then re-emitted as thermal radiation according to the body temperature and Planck's law. The fraction ε of radiation absorbed by the body is called emissivity, and can vary from 0 (all radiation reflected) to 1 (all radiation absorbed). The remaining fraction r is called reflectivity and by the energy conservation law $\varepsilon + r = 1$.

Earth is the body that the remote sensing community is interested in. Earth emissivity depends on the wavelength of the electromagnetic radiation, and it is often termed spectral emissivity. It also depends on the kind of surface, implying a dependence from latitude and longitude. Different types of soil also engender a partial seasonal dependence, in fact barren lands and cultivated fields have different emissivity profiles and snow alters emissivity.

Radiative transfer [1] is the equation that models the intensity of electromagnetic radiation as it travels through a not empty mean. Interferometers that are monitoring the atmosphere from space measure the spectrum, i.e. the intensity of radiation as a function of wavelength, as it is seen by the instrument.

We will focus on instruments measuring in the infra-red spectral band. More precisely, we will consider the Far-infrared Outgoing Radiation Understanding and Monitoring (FORUM) mission [2–4], which will be the 9th Earth-Explorer mission of the European Space Agency with expected launch date in 2027. It will sound the atmosphere in the whole spectral emission band of the Earth, between 100–1600 cm^{-1} (6–100 μm in wavelength), covering the Middle Infra-Red (MIR) and, for the first time, the Far Infrared (FIR) portion, below 650 cm^{-1} (15 μm).

If the atmospheric state is known, the spectrum can be modeled using the radiative transfer equation along the line of sight of the instrument. To obtain an estimate of the atmospheric composition, the radiative transfer equation must be inverted. The inversion of the radiative transfer is also called retrieval.

* Corresponding author.
E-mail addresses: luca.sgheri@cnr.it (L. Sgheri), cristina.sgattoni@cnr.it (C. Sgattoni), chiara.zugarini@fi.iac.cnr.it (C. Zugarini).

https://doi.org/10.1016/j.matcom.2024.10.015
Received 26 June 2024; Received in revised form 30 September 2024; Accepted 11 October 2024
Available online 18 October 2024

The radiative transfer for a layer of a homogeneous non-scattering mean and a single wavelength can be derived from the Lambert–Beer and Planck laws (see for instance [5]) and can be written:

$$\begin{cases} \frac{d}{dz} I(z) = -\alpha I(z) + \alpha B(T) \\ I(z_0) = I_0, \end{cases} \tag{1}$$

where z is the spatial coordinate, $I(z)$ is the intensity of the electromagnetic radiation, T is the temperature of the layer, B is the Planck function and α is the attenuation coefficient, that depends on pressure, temperature and concentrations of the various atmospheric gases in the layer. Eq. (1) has the analytical solution

$$I(z) = I_0 \exp(-\alpha(z - z_0)) + B(T)(1 - \exp(-\alpha(z - z_0))). \tag{2}$$

For a nadir-looking spectrometer mounted on a satellite the radiative transfer equation extends from Earth level z_0 to an altitude z_N of about 120 km that can be considered the top of atmosphere. Above this altitude the density is so low that we can disregard absorption and emission phenomena, and consider the space to be void. If the atmosphere is discretized in homogeneous layers $[z_{i-1}, z_i]$, with T_i and α_i the Curtis-Godson [6] average temperature and attenuation coefficient of the layer i, the corresponding optical depth is $\tau_i = \alpha_i(z_i - z_{i-1})$. Then, if ε and T_E are the emissivity and temperature of Earth surface at the location of the scan, respectively, the solution of the radiative transfer can be written [5]:

$$\begin{aligned} I(z_N) = &\left[\epsilon\ B(T_E) + (1-\epsilon) \left(\sum_{i=1}^{N} B(T_i)\ (1 - e^{-\tau_i})\ e^{-\sum_{j=1}^{i-1} \tau_j} \right) \right] e^{-\sum_{i=1}^{N} \tau_i} \\ &+ \sum_{i=1}^{N} B(T_i)\ (1 - e^{-\tau_i})\ e^{-\sum_{j=i+1}^{N} \tau_j}. \end{aligned} \tag{3}$$

In the retrieval inverse problem under clear sky conditions the unknowns are the surface temperature and the emissivity, as well as the vertical profiles of temperature and concentration of the main atmospheric gases. The temperature and concentrations in (3) are embedded in the attenuation coefficients α_i, but in this paper we only focus on emissivity. Note, however, that having unknowns in the combination of exponentials lead to a severely ill-conditioned problem, see for instance [7,8].

One of the most common methods for inverting the radiative transfer is the Optimal Estimation (OE) method by Rodgers [7], that combines in a Bayesian approach two mathematical techniques.

1. The use of a weighted L^2 norm for calculating the error between the instrumental and simulated spectra;
2. The use of a Tikhonov penalization term, using the weighted L^2 norm of the difference between the retrieved profiles and a given a priori.

Let $\mathbf{x}$, $\mathbf{F}$ and $\mathbf{y}$ be the state vector of the parameters of the retrieval problem, the forward model at each wavenumber and the vector of the spectrum measured by the instrument, respectively. If we suppose that the $\mathbf{y}$ measurements are random variables with a Gaussian experimental error, we can define the Variance–Covariance Matrix (VCM) of the measurements as

$$\mathbf{S}_y = \mathbb{E}((\mathbf{y} - \mathbb{E}(\mathbf{y}))(\mathbf{y} - \mathbb{E}(\mathbf{y}))^t), \tag{4}$$

where $\mathbb{E}$ is the expected value. If we have a model $\mathbf{x}_a$ for the parameters $\mathbf{x}$ and we know the variability of the a priori, we can also define the VCM $\mathbf{S}_a$ of the a priori in the same way. The a priori $\mathbf{x}_a$ may come for instance from the climatology or from correlated measurements. The OE method consists in minimizing the following functional:

$$\chi^2(\mathbf{x}) = (\mathbf{y} - \mathbf{F}(\mathbf{x}))^t \mathbf{S}_y^{-1} (\mathbf{y} - \mathbf{F}(\mathbf{x})) + (\mathbf{x}_a - \mathbf{x})^t \mathbf{S}_a^{-1} (\mathbf{x}_a - \mathbf{x}). \tag{5}$$

The calculation of the attenuation coefficients is a heavy computational task, because it involves obtaining information from a spectroscopic database such as the HIgh resolution TRANsmission (HITRAN) 2020 database, see [9]. On the other hand, the calculation of the Jacobian of $\mathbf{F}$ with respect to $\mathbf{x}$ is easily obtained because of the exponential dependence. Thus, the minimization is normally carried out using an analytical method such as the Gauss–Newton (GN) method with the Levenberg–Marquardt technique to counter the non-linearity of the problem.

There are several issues in the retrieval of spectral emissivity. First, there are bands where the absorption lines of atmospheric gases mask the signal from the Earth's surface. For instance, in the 300-600 cm^{-1} interval the absorption lines of water vapor make the atmosphere opaque unless we are at polar latitudes, where the atmosphere is very dry [10]. On the other hand, in the MIR region we have two atmospheric windows, roughly corresponding to 800-950 cm^{-1} and 1020-1200 cm^{-1} intervals. In these frequency ranges the atmosphere in clear-sky conditions is highly transparent because there are very few absorption lines, so that surface parameters (temperature and emissivity) can be retrieved. For a recent study of the emissivity sensitivity in the FORUM spectral range see [11].

Secondly, in the radiative transfer (3) the dependence of the spectrum $I(z_N)$ on ε is linear. In the atmospheric windows, where there is the maximal sensitivity to emissivity, the Planck function can also be approximated with a straight line with negative slope, since the maximum of the Planck function for attainable surface temperatures is reached around 600 cm^{-1}. Thus, also the dependence of the spectrum on the surface temperature is almost linear, and this leads to negative covariances between the two parameters [12,13]. The anti-correlation can reach values of −0.8 in the atmospheric windows [4]. Note that this is only a mathematical correlation due to the form of the radiative transfer equation, it does not imply any physical correlation between surface temperature and emissivity.

There are different ways of tackling this problem, to avoid biases in the retrieved surface temperature and spectral emissivity. We list here some techniques.

1. Changing the spectral grid of the emissivity. From Eq. (3) we note that, while $B(T_E)$ depends via the Planck function on the single value T_E, we could define a different ϵ for each measurement. Due to the experimental errors, the emissivity profile cannot be reconstructed pointwise, but we need to reduce the number of variables by applying a linear spline interpolation over the spectral grid as commonly used.
   A coarser grid reduces the random noise, since a single value averages more spectral measurements, but fine features of real emissivity cannot be reproduced. On the other hand a finer grid has a larger random noise, but in principle can reproduce the small-scale features that are present in some emissivity profiles.
2. Changing the $\mathbf{S}_a$, for instance by assigning a larger noise than expected, permits larger variations of emissivity in the iterations of the GN sequence. Also, reducing or eliminating the correlations in the $\mathbf{S}_a$ permits a sharper definition of the emissivity profile in the transition zones of the sensitivity regions. However, a weaker regularization may trigger unwanted oscillations in the retrieved emissivity profile. An a-posteriori regularization such as the Iterative Variable Strength (IVS) [14,15] may be needed to reduce this phenomenon.
3. Using the geolocation and time of the scan allows to determine a more accurate prediction of the emissivity profile to be used as initial guess or a priori with respect to the typical fixed initial values of 0.9 or 0.99.

The first two techniques are considered in [4] for FORUM retrievals, though a more complete study would be desirable, especially when the final specifications of the instrument are fully defined. In this paper we study the third issue, i.e. finding an a priori statistically closer to the truth using emissivity models and climatological data.

Naturally, using a priori values that are closer to the true ones generally provides an advantage in minimizing the OE functional [16], as it reduces the bias in the solution introduced by errors in the a priori values.

To demonstrate that an emissivity profile closer to the true values can indeed help addressing the anti-correlation issue, we repeated the retrieval for case 1.1 (clear sky desert at noon) from [4] in the appendix. This case exhibited the largest error in the retrieval of surface temperature and emissivity due to their large anti-correlation.

Other instruments also use geolocated information for the emissivity. For example, the IASI (Infrared Atmospheric Sounding Interferometer) sounder uses the PWLR[3] (Piece-Wise Linear Regression) fast algorithm to perform statistical retrievals in all sky conditions. Under clear sky conditions, these data are then used for a subsequent retrieval using the Optimal Estimation method [17].

Similarly, the Atmospheric InfraRed Sounder (AIRS) [18] relies on a preliminary retrieval from the onboard AMSU sensor [19,20] which uses an a priori emissivity based on soil classification. In the latest version of its retrieval algorithm, the emissivity profile is kept fixed over water but is retrieved at certain hinge points over land.

Finally, the CRoss-track Infrared Sounder (CRIS) instrument [21] uses the onboard Visible Infrared Imaging Radiometer Suite (VIIRS) sensor and its surface reflectance product [22].

2. Emissivity models and climatologic datasets

2.1. Huang set of profiles

There are different models for emissivity profiles as a function of the type of surface. The Huang profiles [23] are very detailed, cover the whole FORUM range, and they have a resolution of $1\ \mathrm{cm}^{-1}$. In this paper we add a profile for tropical to middle latitude forests to the set of eleven Huang profiles used in the FORUM E2E simulator [4]. The surface types of the Huang profiles selected are reported in Table 2 of Section 3. In our technique we only use the set of Huang profiles, and not the emissivity databse created by Huang, which on the other hand will be used in Section 4 for comparison.

2.2. Emissivity databases

In this paper we consider the following emissivity databases.

1. The MODerate resolution Imaging Spectroradiometer (MODIS) database from the University of Wisconsin [24,25] is available online from the site: https://lpdaac.usgs.gov. The MOD11 products consist in monthly means of emissivity at the following 10 wavelengths: 3.6, 4.3, 5.0, 5.8, 7.6, 8.3, 9.3, 10.8, 12.1, and 14.3 μm with 0.05° spatial resolution.
2. The Jet Propulsion Laboratory produces a Global Emissivity Dataset (GED) using the Advanced Spaceborne Thermal Emission and Reflection (ASTER) Radiometer [26,27], available from https://emissivity.jpl.nasa.gov/aster-ged. The ASTER GEDv3 contains five emissivity values in the TIR band at multiple resolutions: 100 m, 1 km and 5 km.
3. The Combined ASTER MODIS Emissivity over Land (CAMEL) database [28,29], which is a combination of the two previous databases.

The properties of these databases are summarized in Table 1

All these databases rely on the concept of *hinge points*, the points that should permit to obtain a good approximation of the emissivity profile using linear interpolation in between. Alternatively, a high resolution emissivity profile can be determined using principal components [30]. For our tests, we will use both the MODIS and the CAMEL databases. In the MODIS database, 6 out of

Table 1
List of emissivity databases considered in this paper with properties.

DB	Periodicity	Resolution	#Values/in FORUM range	Values in FORUM range [cm^{-1}]
MODIS	Monthly	0.05°	10/6	699, 826, 925, 1075, 1204, 1315
ASTER	Monthly	100 m, 1 km, 5 km	5/5	884, 943, 1098, 1162, 1204
CAMEL	Monthly	0.05°	13/9	699, 826, 884, 925, 943,1098, 1162, 1204, 1315

Table 2
List of acronyms for Huang emissivity profiles, and ancillary data constraints used. Snow cover larger than 50% flag, surface temperature and humidity admissible ranges.

ACR	SOIL TYPE	SNOW	TSKIN	HUMID
DES	Desert	N	≥ 20 °C	≤ 20%
D&G	Desert 45% and grass 55%	N	≥ 0 °C	≤ 25%
GRS	Grass	N	–	10%–45%
DGR	Dry grass	N	–	≤ 35%
DEC	Deciduous	N	–	10%–35%
CON	Conifer	N	–	20%–45%
WAT	Water	N	≥ −6 °C	–
FSN	Fine snow	Y	–	–
MSN	Medium snow	Y	–	–
CSN	Coarse snow	Y	–	–
ICE	Ice	Y	≤ −6 °C	–
FOR	Forest	N	≥ 4 °C	≥ 40%

the 10 emissivity values are included in the FORUM spectral range. In the CAMEL database, 9 out of the 13 emissivity values are included in the FORUM spectral range.

Finally Huang [23] also assembled an emissivity database with monthly average values, using its own profiles and MODIS data to determine the soil type. The validation is made using IASI retrieved emissivities.

2.3. Atmospheric and ancillary data

The ECMWF (European Center for Medium range Weather Forecast) Re-Analysis ERA5 database [31], available at https://www.ecmwf.int/en/forecasts/dataset/ecmwf-reanalysis-v5, contains a source of atmospheric states, obtained with the assimilation of measurements from many different instruments. The ERA5 version contains a hourly database of geolocated vertical profiles of pressure, temperature, water vapor and ozone content on a 0.25° grid in latitude and longitude. On the same grid surface temperature and pressure are available. Additional gas concentrations for CO_2, CO, CH_4, NO_2, HNO_3, SO_2 are taken from the CAMS (Copernicus Atmosphere Monitoring Service) global Greenhouse Gas reanalysis (EGG4) [32], available at https://ads.atmosphere.copernicus.eu/datasets/cams-global-ghg-reanalysis-egg4-monthly. Missing atmospheric gas profiles are taken from the Initial Guess 2 (IG2) databases [33].

Ancillary data that will be used in our setting are the monthly snow cover fraction and soil humidity percentage [34]. While NRT (Near Real Time) maps are available, for instance from https://www.nohrsc.noaa.gov/nh_snowcover/, in this study we only use climatology. In the ERA5 database there is a soil type parameter which is linked to the soil texture. However, a very detailed map of soil types with a resolution of 0.05° in latitude and longitude is the MODIS/Terra+Aqua Yearly Land Cover Type database available from https://doi.org/10.5067/MODIS/MCD12C1.006 [35].

3. Methodology

Our key point is to make use of the high-resolution Huang emissivity profiles, that are based on accurate measurements, as explained in [23], while linking the selection to the available emissivity measurements and ancillary data. We propose two approaches, the first one is based on empirical constrains on ancillary data but no information about the soil type is used as an a priori. In the second approach, the information about the soil type is mapped to the relevant point, using a Bayesian approach.

3.1. Selection of profiles via ancillary data

The ancillary data that will be used as constrains are reported in Table 2.

1. The snow cover. If the fraction is larger than a threshold, then snow/ice profiles instead of land profiles will be used. We set the threshold to 50%. The snow cover is only available over land.
2. The surface temperature. This will be used to impose some restrictions on the profiles, but mainly to distinguish pure water from ice on geolocations that are located over the oceans. While the freezing point of ocean water starts at −1.8 °C [36], the fraction and depth of ice depends on how long and how lower than the freezing point the temperature remains. Since on the sea we have no emissivity data, we set a threshold value of −6 °C to distinguish water from ice. Also, some mild constrains are used for some particular type of soils.

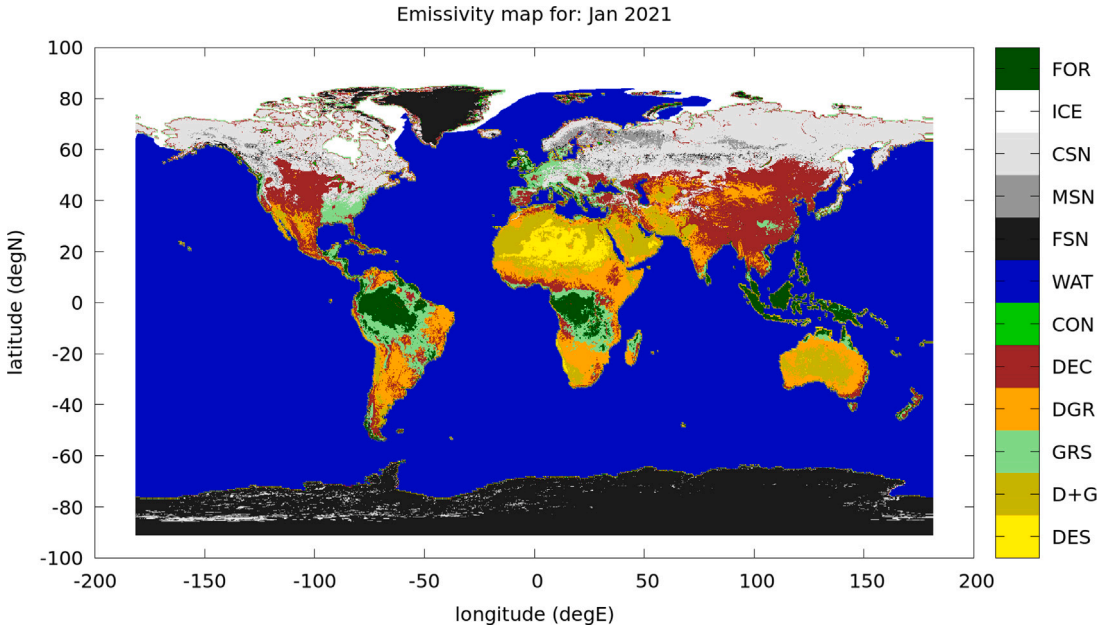

Fig. 1. Map of selected Huang profiles for January 2021.

3. The soil humidity. Here again some empirical considerations were used to exclude arid soil types if the humidity is high. Also, the forest profile is expected to have a high humidity.

Again, we stress that this choice only determines the a priori for the emissivity profile, the retrieved profile is determined by inverting the radiative transfer equation. Except for the freezing point of water, the thresholds were set empirically by analyzing the database values of surface temperature and humidity across different regions of Earth.

For each ERA5 grid point, we select the soil types that do not violate the constraints reported in Table 2, and then choose within this set the one with the minimal Root Mean Square Error (RMSE) in emissivity with respect to the MODIS database. On water, when there is no MODIS data, the profile is decided by the surface temperature. The results are shown in Fig. 1 for January 2021, and in Fig. 2 for July 2021.

Both maps are defined in the $[-85°, 85°]$ latitude range, so the Summer polar North ice cap does not appear. Note that the snow covering is the only parameter linked to the soil type that is used in this identification.

In Fig. 3 we report the average RMSE with respect to the MODIS data in July. A similar plot holds also for January. In the left panel we show the error in the case of the selected Huang profile, in the right panel the error in case a constant emissivity equal to 0.99 is selected. From the figure we note that selecting an appropriate Huang profile reduces the initial error as expected. Even in the case of the Huang profiles, there is a residual noticeable error mostly concentrated in the arid zones. This is due to the fact that there is a large variability in the desert emissivity, due to the presence of the quartz Reststrahlen bands in the sandy areas [30,37] but not in the rocky areas. We also repeated the method using the CAMEL data. The results are very similar, so we skip presenting them.

3.2. Selection of profiles via Bayesian approach

We use the Huang profiles on a $\nu_k = 50 + 5(k-1)$ set of wavenumbers, $k = 1, \dots, 321$. This set covers the $[50, 1650]$ cm^{-1} band at a resolution of 5 cm^{-1}, an interval sufficient to calculate the simulated FORUM spectra. In this approach we search an optimal estimation profile $e(\nu)$ as a convex combination of the Huang profiles $H = \{H_i(\nu),\ i = 1, \dots, 12\}$.

$$e(\nu) = \sum_{i=1}^{12} p_i H_i(\nu), \quad p_i \geq 0, \quad \sum_{i=1}^{12} p_i = 1 \tag{6}$$

We define an a priori for the emissivity making use of the MODIS/Terra+Aqua Yearly Land Cover Type database in [35], that contains a static estimate of the type of soil with a 0.05° grid in latitude and longitude. The 17 soil types considered are different from those considered by the Huang profiles, they are listed in Table 3.

We established a correspondence matrix $\mathbf{M}$ between the soil types in the land cover map and the Huang emissivity profiles. Let $T = \{T_l,\ l = 1, \dots, 17\}$ represent the soil types of the database in [35]. We define an equivalence mapping from the set T of soil types to the set H of emissivity profiles. Let $\mathbf{M} = (m_{ij})$ be a 17×12 matrix, where each MODIS soil type i is assigned a probability m_{ij} for

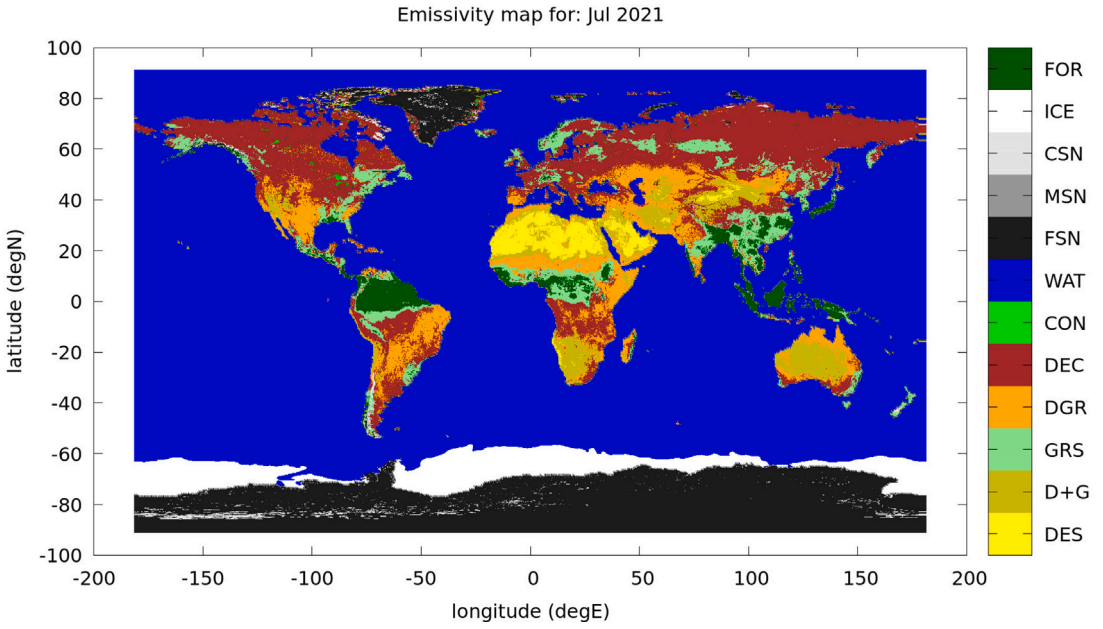

Fig. 2. Map of selected Huang profiles for July 2021.

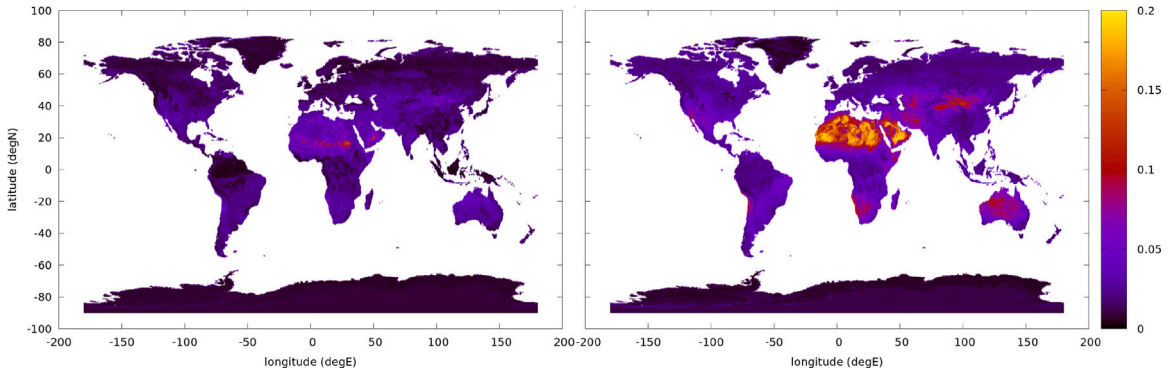

Fig. 3. RMSE with respect to MODIS data for July 2021. Left panel (selected Huang profiles), right panel (constant emissivity 0.99).

Table 3
Definition of the 17 land cover types.

1	Barren or sparsely vegetated	2	Snow and ice
3	Cropland/natural vegetation mosaic	4	Urban and built-up
5	Croplands	6	Permanent wetlands
7	Grasslands	8	Savannas
9	Woody savannas	10	Open shrublands
11	Closed shrubland	12	Mixed forests
13	Deciduous broadleaf forest	14	Deciduous needleleaf forest
15	Evergreen broadleaf forest	16	Evergreen needleleaf forest
17	Water		

each Huang profile j. Here, $m_{ij} \geq 0$, and $\sum_j m_{ij} = 1$ for every i. The actual matrix $\mathbf{M}$ is shown in Table 4. This correspondence was empirically established based on the descriptions of the MODIS soil types, excluding any Huang profiles that were incompatible. The remaining Huang profiles were assigned probabilities according to their similarity to the MODIS soil types. For each ERA5 grid point, we calculated the probability of each of the 17 soil types by averaging the points that would be enclosed in the FORUM field of view, if the center of the FORUM pixel were the ERA5 grid point, i.e. points with a distance less of equal 7.5 km from the center. This method provides a global sample of emissivities on the same grid as the ERA5 data.

Table 4
Correspondence between Land Cover Map and Huang profiles.

LT	DES	D+G	GRS	DGR	DEC	CON	WAT	FSN	MSN	CSN	ICE	FOR
1	0.5	0.3	0	0.2	0	0	0	0	0	0	0	0
2	0	0	0	0	0	0	0	0.25	0.25	0.25	0.25	0
3	0	0	0.5	0	0.5	0	0	0	0	0	0	0
4	0	0	0.1	0.1	0.8	0	0	0	0	0	0	0
5	0	0	0.1	0	0.9	0	0	0	0	0	0	0
6	0	0	0.2	0	0	0	0.8	0	0	0	0	0
7	0	0	0.8	0	0.1	0	0	0	0	0	0	0.1
8	0	0.2	0.4	0.2	0.2	0	0	0	0	0	0	0
9	0	0	0.3	0	0.3	0	0	0	0	0	0	0.4
10	0	0	0	0	0.6	0.2	0	0	0	0	0	0.2
11	0	0	0	0	0.4	0.3	0	0	0	0	0	0.3
12	0	0	0	0	0.2	0.4	0	0	0	0	0	0.4
13	0	0	0	0	0.5	0	0	0	0	0	0	0.5
14	0	0	0	0	0.5	0.5	0	0	0	0	0	0
15	0	0	0	0	0	0	0	0	0	0	0	1
16	0	0	0	0	0	1	0	0	0	0	0	0
17	0	0	0	0	0	0	1	0	0	0	0	0

Then, if t_l are the fractions of the T_l soils in the FORUM pixel, we can find an a priori emissivity profile by defining:

$$H_a(\nu) = \sum_{l=1}^{17} t_l \sum_{j=1}^{12} m_{lj} H_j(\nu). \tag{7}$$

We can group the coefficients of the Huang profiles, defining $a_i = \sum_{l=1}^{17} t_l m_{li}$. Then, (7) can be recast as:

$$H_a(\nu) = \sum_{i=1}^{12} a_i H_i(\nu), \tag{8}$$

where $a_i \geq 0$, $\sum_i a_i = 1$.

The optimal emissivity profile should not be far from the a priori. However, the optimal emissivity profile should also be compatible with the chosen emissivity database. For this experiment we selected the CAMEL database. Let n_j and $e_j^{(k)}$ $j = 1, \dots, 9$ the CAMEL wavenumbers and monthly emissivity values for an ERA5 grid point k that are inside the FORUM spectrum. Let $\bar{e}_j$ the average value of the $e_j^{(k)}$, then:

$$\mathbf{S}_{C\,ij} = \frac{1}{N} \sum_{k \in \text{ERA5 grid}} (e_i^{(k)} - \bar{e}_i)(e_j^{(k)} - \bar{e}_j) \tag{9}$$

is the experimental VCM of the CAMEL emissivities calculated on the set of N ERA5 grid points.

Let $\bar{h}_j$ be the average of the 12 Huang profiles for the wavenumber ν_j, $j = 1, \dots, 321$. We can calculate the Huang VCM as:

$$\mathbf{S}_{H\,ij} = \frac{1}{12} \sum_{k=1}^{12} (H_k(\nu_i) - \bar{h}_i)(H_k(\nu_j) - \bar{h}_j). \tag{10}$$

However, this 321×321 matrix does not really represent the real variability of the Huang profiles, because the correlation between adjacent points is very large. Thus, we use the technique of McMillin and Goldberg [38], also used by Matricardi [39] for the IASI (Infrared Atmospheric Sounding Interferometer) sounder, to reduce the cardinality of the VCM. We first select the wavenumber $\bar{\nu}_1 = \nu_{j_1}$ as the one with the largest standard deviation, i.e. $\mathbf{S}_{H\,j_1 j_1} \geq \mathbf{S}_{H\,ii}$, $\forall i$. Then we discard all wavenumbers ν_l such that:

$$|\mathbf{S}_{H\,j_1 l}| \geq c \sqrt{\mathbf{S}_{H\,j_1 j_1} \mathbf{S}_{H\,ll}} \tag{11}$$

for some constant $0 < c < 1$ and repeat the procedure until all additional wavenumbers are removed. In this way we select a subset of wavenumbers ν_{j_l}, $l = 1, \dots, L$ (the *super channels* in the original terminology) that is representative of the variability of the Huang profiles.

The result of the procedure with $c = 0.9$ is reported in Fig. 4, where we obtain $L = 15$. This value was selected because they well represent the hinge points of the Huang emissivity profiles. Let us define $\mathbf{S}_R$ the $L \times L$ VCM obtained taking the set of j_l rows and columns from $\mathbf{S}_H$. Thus, if we suppose that both the difference from the CAMEL data and from the a priori are random Gaussian variables, the combined probability of finding an optimal profile $e^{(k)}(\nu) \equiv \sum_i p_i^{(k)} H_i(\nu)$ for the ERA5 grid point k is:

$$\begin{aligned} p(e^{(k)}(\nu)) = & \frac{\det(\mathbf{S}_C)^{-1/2}}{(2\pi)^{-9/2}} \exp\left(-\frac{1}{2}(\mathbf{e}^{(k)}(\mathbf{n}_C) - \mathbf{e}_C^{(k)})^t \mathbf{S}_C^{-1} (\mathbf{e}^{(k)}(\mathbf{n}_C) - \mathbf{e}_C^{(k)})\right) \\ & \cdot \frac{\det(\mathbf{S}_R)^{-1/2}}{(2\pi)^{-L/2}} \exp\left(-\frac{1}{2}(\mathbf{e}^{(k)}(\mathbf{n}_R) - \mathbf{e}_R^{(k)})^t \mathbf{S}_R^{-1} (\mathbf{e}^{(k)}(\mathbf{n}_R) - \mathbf{e}_R^{(k)})\right), \end{aligned} \tag{12}$$

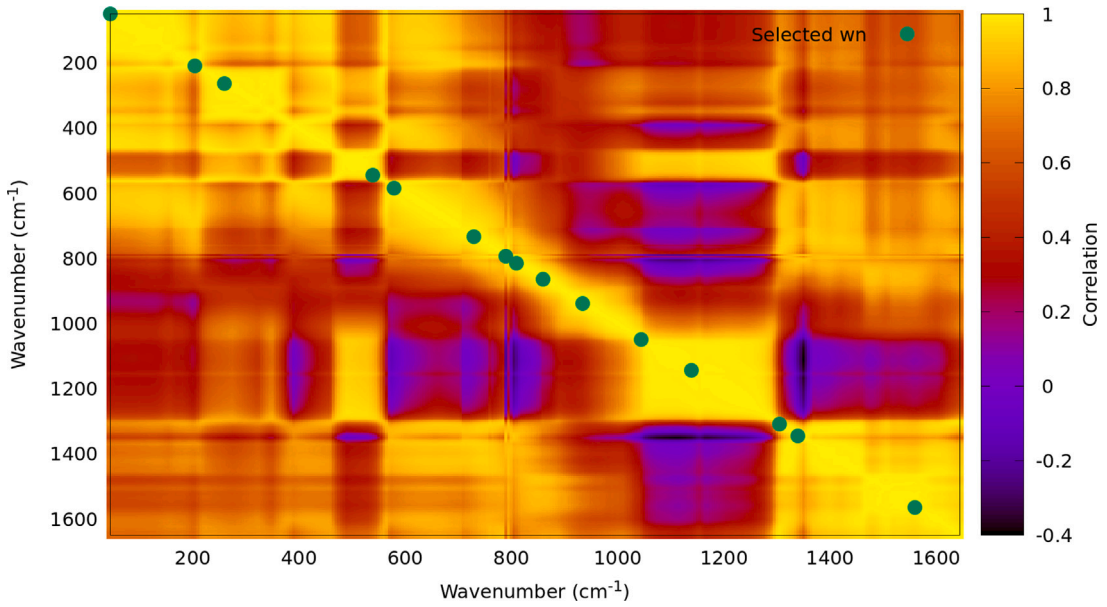

Fig. 4. Correlation matrix for the set of Huang profiles and selected wavenumbers.

where $\mathbf{n}_C$ is the vector of the 9 CAMEL wavenumbers n_j included in the FORUM spectral range, $\mathbf{n}_R$ is the vector of the L reduced set of Huang wavenumbers ν_{j_l}, $\mathbf{e}_C^{(k)}$ is the vector of CAMEL emissivities for the k ERA5 grid point, $\mathbf{e}_R^{(k)}$ is the vector of the a priori Huang emissivities H_a on the $\mathbf{n}_R$ vector, and finally $\mathbf{e}^{(k)}(\mathbf{n}_C)$ and $\mathbf{e}^{(k)}(\mathbf{n}_R)$ are the values of the $e^{(k)}(\nu)$ function defined in (6) on the vectors $\mathbf{n}_C$ and $\mathbf{n}_R$, respectively. The probability of (12) can be maximized by minimizing the sum of the exponents:

$$\begin{aligned} J(p_1,\dots,p_{12}) &= (\mathbf{e}(\mathbf{n}_C)-\mathbf{e}_C)^t\mathbf{S}_C^{-1}(\mathbf{e}(\mathbf{n}_C)-\mathbf{e}_C) \\ &+ (\mathbf{e}(\mathbf{n}_R)-\mathbf{e}_R)^t\mathbf{S}_R^{-1}(\mathbf{e}(\mathbf{n}_R)-\mathbf{e}_R), \end{aligned} \tag{13}$$

where for simplicity we dropped the dependence from k in the notation. The functional (13) has the obvious constrains $p_i \geq 0$, $\sum_i p_i = 1$, see (6). If the minimization were carried out on all p_i, the minimization would insert profiles that are not compatible with the geolocation in order to minimize the distance from the CAMEL data, for instance snow profiles in the tropics. To avoid this problem, the minimization is carried out only on the Huang profiles contained in the a priori, that is profiles i such that $a_i > 0$ in (8). The functional J is a quadratic function of the p_i, so (13) can be solved explicitly with the constrained linear least-square method.

4. Test of the method on experimental IASI data

The IASI (Infrared Atmospheric Sounding Interferometer) sounder [40] is a Fourier transform interferometer that measured atmospheric spectra since 2006. The IASI interferometer swath includes 30 Fields of Regard (FoR). Each FoR consists of 4 Fields of View (FoV) that are acquired simultaneously. Each FoV corresponds to a spectrum. The different FoRs have different nadir angles. The land covered by each swath is a strip about 2200 km wide perpendicular to the IASI orbit. To avoid the influence of the observation angles that distort the shape of the FoV, we only selected the two central FoRs, which have an inclination not larger than 8° with respect to the nadir. The shape of these FoVs is roughly circular with a 12 km diameter. Moreover, we discarded FoVs over water and FoVs that are considered cloudy. The IASI FoVs considered have their own geolocation, which can be read from the IASI Level 2 files.

For the comparison tests we used the emissivity data available in the IASI Level 2 products provided by EUMETSAT Data Services [17], which are available online from the site: https://pn-ui.prod.wekeo2.eu/pn-ui/start. The emissivity values in the IASI products are given for the following channels: 765, 900, 991, 1071, 1160, 1228, 1980, 2111, 2170, 2510, 2634, and 2760 cm^{-1}. We only consider the first 6 wavenumbers, as they fall into the FORUM spectral range.

To conduct the tests consistently with the datasets used in the generation of the ERA5 grid, we selected orbits from January and July 2021; specifically, we considered the orbits from July 15th and 16th, and some orbits from January 16th, 19th, and 20th. To determine coincidences between the ERA5 grid, on which both the CAMEL and the Bayesian profiles are based, and the IASI FoVs, we set a tolerance of ±0.05° for longitude and latitude between the center of the IASI FoV and the ERA5 grid point. Using these criteria, we obtained a sample of 4530 coincidences for January and 4480 coincidences for July.

To assess the Bayesian method of Section 3.2, we compared the RMSE of the difference between the Bayesian test (labeled BAYES) and the IASI data, and the RMSE of the difference between the CAMEL profile, obtained by interpolating the CAMEL values, and

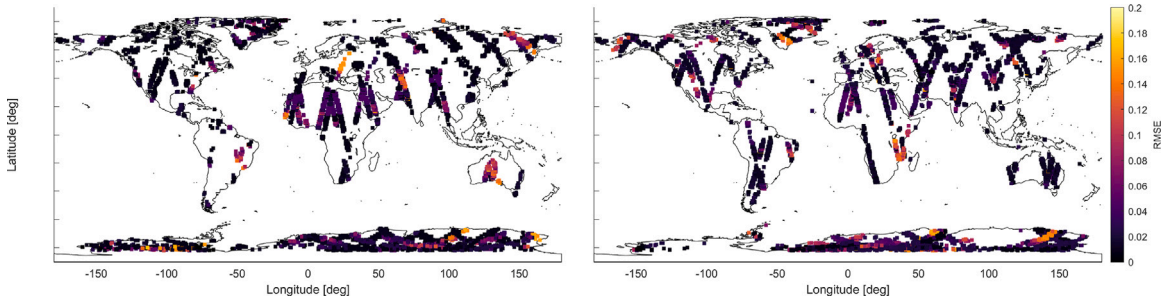

Fig. 5. RMSE of the emissivity of BAYES-IASI. Left panel January, right panel July.

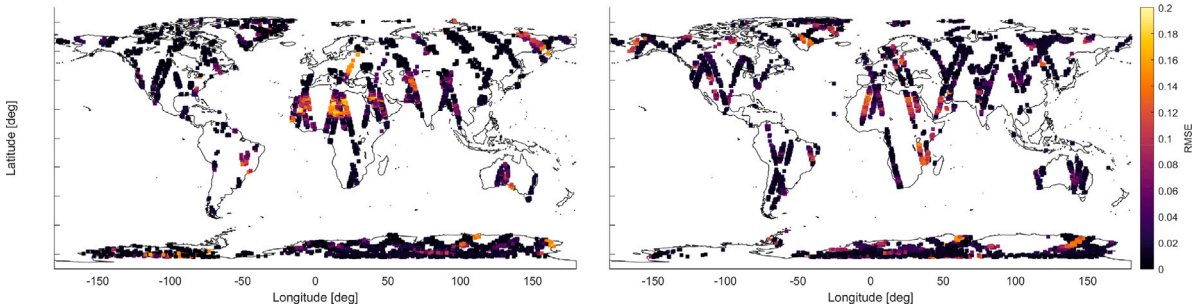

Fig. 6. RMSE of the emissivity of CAMEL-IASI. Left panel January, right panel July.

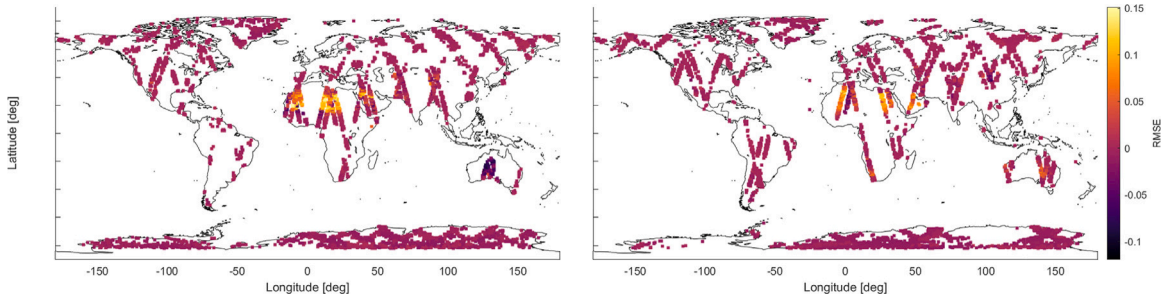

Fig. 7. Differences between CAMEL-IASI RMSE and Bayesian-IASI RMSE. Left panel January, right panel July.

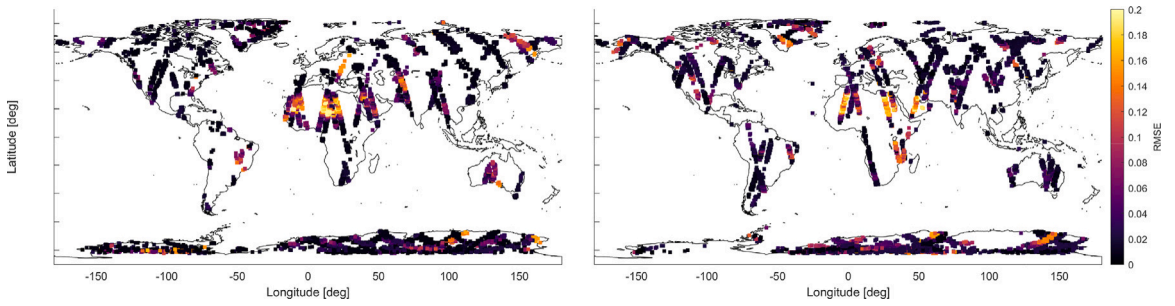

Fig. 8. RMSE of the emissivity of HUANG-IASI. Left panel January, right panel July.

the IASI data. We also took into consideration the Huang database of emissivities [23] (labeled HUANG). The HUANG emissivity database is first calculated on a fine grid of $0.05° \times 0.05°$, where an individual Huang profile is selected based on its best agreement with MODIS data. The results are then averaged on a final $0.5° \times 0.5°$ grid in a second step, where the weights of the Huang profiles are statically determined by the number of occurrences of the profiles in the final grid.

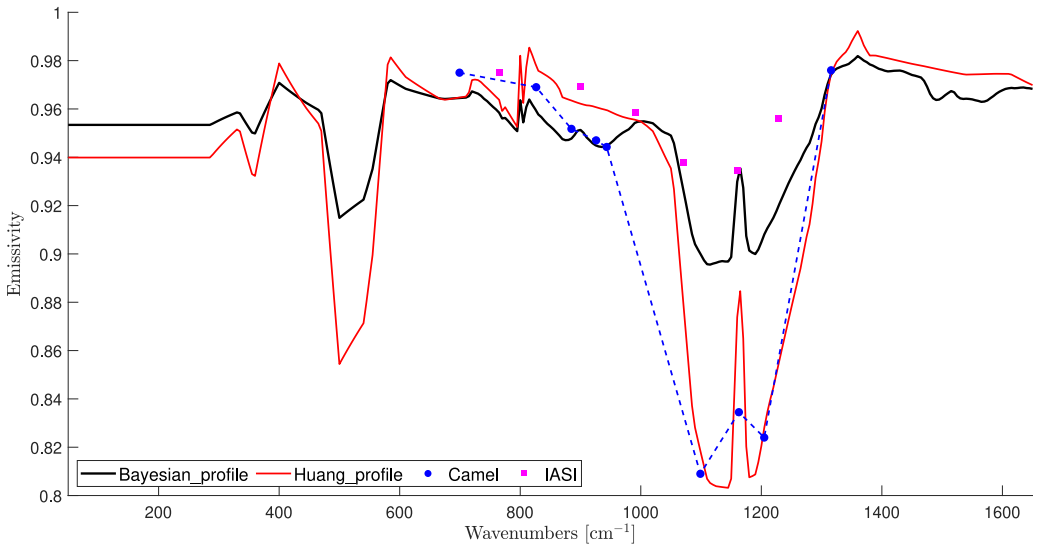

Fig. 9. Sahara desert (lat=22N, lon=16.5E) emissivity reconstruction. Purple squares (IASI data), dotted blue line (CAMEL interpolated profile), red line (HUANG profile), black line (BAYES profile).

Table 5
Average RMSE of the differences between the BAYES solution, the CAMEL profiles and the HUANG database versus the IASI data. Also, difference between CAMEL and BAYES solutions.

	January	July
BAYES-IASI	0.0264	0.0285
CAMEL-IASI	0.0297	0.0300
HUANG-IASI	0.0333	0.0350
CAMEL-BAYES	0.0191	0.0147

In Figs. 5 and 6 and we show the results of the test for the months of January (left panel) and July (right panel). In Fig. 7 we also report the difference in the RMSE between the two tests, to highlight the improvements of our method. We note that the Bayesian test agrees better with the IASI data over Africa for both months, while there is a worsening over Australia in the January test.

Finally, in Fig. 8 we also report the difference between the HUANG database and the IASI data.

Table 5 summarizes the results, reporting the average RMSE of the various tests with respect to the IASI data, calculated on the samples. From the second row we note that the IASI and CAMEL data are not fully compatible. This has to be expected, since the CAMEL data are monthly mean on a grid with $0.25°$ step, while the IASI data refers to a FoV that is 12 km in diameter. We note that our Bayesian method finds a solution which is not far from the CAMEL data (last row), but agrees better with the experimental IASI data both with respect to the CAMEL and the HUANG solutions.

The BAYES method is closer to the IASI data than the CAMEL interpolated profile, that nevertheless reconstruct exactly the values of the CAMEL database. An example of the reconstructed profiles is shown in Fig. 9. The improved performance of the BAYES method is likely due to the combination of two factors:

1. The a priori information in the BAYES method is derived from MODIS/Terra+Aqua data, which provides a detailed description of soil types on a very fine grid. This allows for a corresponding combination of Huang profiles that approximates the true emissivity values well. This approximation is then further refined by minimizing (13) using CAMEL data.
2. The CAMEL solution does not account for small-scale features that cannot be deduced from CAMEL's sampling. In contrast, the BAYES solution is determined as a convex combination of high-resolution profiles, which retain small-scale features of soil types that are generated from accurate measurements.

The BAYES method is also closer to the IASI data than the HUANG emissivity database. Both methods use an emissivity database and the same set of profiles to build the emissivity. However, we additionally rely on the MODIS/Terra+Aqua Yearly Land Cover Type data to construct an a priori profile. The final profile is then selected as a convex combination of Huang profiles, by maximizing the joint probability of being close to both the a priori and the CAMEL measurements. By using these two constraints within a single optimization step, the method allows for a more flexible determination of the optimal emissivity profile, resulting in a closer alignment with experimental data.

Finally, we calculated the significance of the deviation from the CAMEL data of the BAYES solution, using a two-sample t-test. The decrease in the RMSE is significant for both the January and the July test. For the January test the probability that the CAMEL

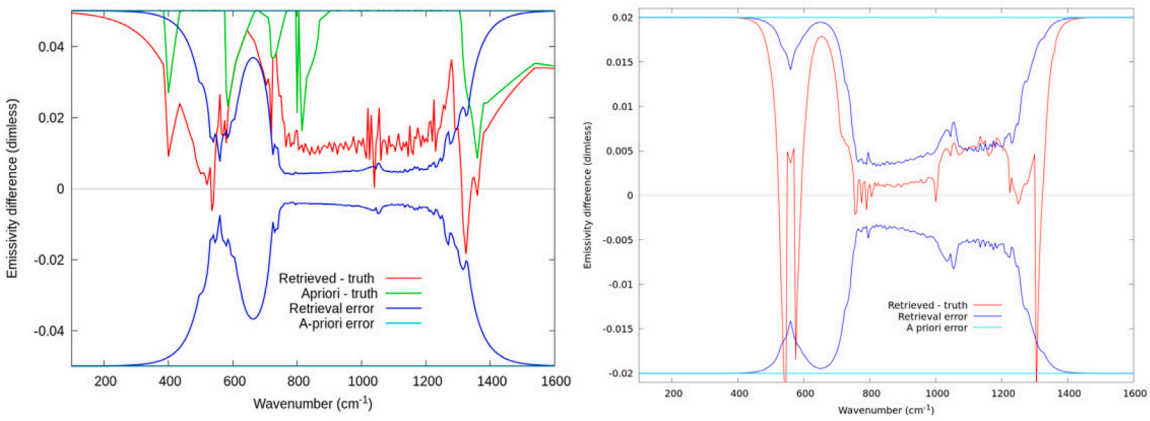

Fig. 10. Retrieval over desert. Left panel: standard E2E settings, right panel: emissivity initial guess and a priori closer to the truth.

sample is drawn from a distribution with an average RMSE lower or equal that of the BAYES sample is $6 \cdot 10^{-6}$. For the July test the value is $2.7 \cdot 10^{-2}$. Both numbers are statistically significant, the larger July value is due to a slightly worse agreement between BAYES and IASI data in that month.

5. Conclusions

In this paper we studied the problem of selecting an emissivity profile that is as close as possible to the experimental data for that geolocation and time. This is important in the retrieval step, because in the radiative transfer equation the dependence of emissivity and surface temperature is very similar, so that assessing both quantities may lead to biases.

We tested two methods for determining an emissivity profile for each geolocation. The first one only uses MODIS and ancillary data that do not include any land cover information, but is still able to obtain a plausible soil type map. The second method is a Bayesian approach that uses the CAMEL database and a detailed land cover map to obtain an emissivity profile in the form of a convex combination of the Huang profiles.

The main result of this paper is that, in the test with IASI experimental data, the Bayesian method performs better than the linear spline obtained by interpolating the CAMEL measurements.

From the point of view of applications, the Bayesian method for determining the emissivity profile is not computationally time-demanding; the generation of a single case profile takes milliseconds on a standard PC. In the future, using this method to determine the initial guess and/or the a priori for the emissivity should reduce the bias in the retrieval of surface parameters.

CRediT authorship contribution statement

Luca Sgheri: Writing – review & editing, Writing – original draft, Software, Methodology, Formal analysis. **Cristina Sgattoni:** Writing – review & editing, Writing – original draft, Software, Formal analysis. **Chiara Zugarini:** Writing – review & editing, Writing – original draft, Software, Formal analysis.

Acknowledgments

The paper originated from a talk at the IMACS 2023 world congress. The project was supported by the CNR, Italy project DIT.AD012.168 *Support to the FORUM mission*. The authors wish to thank INdAM mathematical research groups GNCS and GNAMPA for support.

Appendix. Retrieval on the desert with an emissivity a priori closer to the true value

In Fig. 10, the left panel shows the retrieval results for case 1.1 from [4] (clear sky desert at noon), using the standard E2E settings. In this case, the emissivity a priori and initial guess is the true value plus 0.05, constrained at 1. The right panel shows the results of the same retrieval, but with an emissivity a priori and initial guess set to the true value plus 0.02. This value is consistent with the error found using our method. Note that in both cases the final reduced χ^2 value is around 1.1, meaning there is no significant improvement in the precision of the reconstruction. However, the actual emissivity error is now smaller, and aligns statistically with the retrieval error calculated through linear error propagation. Additionally, the retrieval error for surface temperature is reduced from -0.815 to -0.13.

References

[1] S. Chandrasekhar, Radiative Transfer, Courier Corporation, 1960.
[2] L. Palchetti, G. Bianchini, M. Brindisi, B. Carli, F. Castagnoli, M. Del Guasta, M. De Laurentis, P. Di Girolamo, F. Esposito, F. Falcini, et al., FORUM: a FORward-looking imaging spectrometer for observation of the environment, Remote Sens. Environ. 216 (2018) 474–491.
[3] L. Palchetti, H. Brindley, R. Bantges, S.A. Buehler, C. Camy-Peyret, B. Carli, U. Cortesi, S. Del Bianco, G. Di Natale, B.M. Dinelli, D. Feldman, X.L. Huang, L. C.-Labonnote, Q. Libois, T. Maestri, M.G. Mlynczak, J.E. Murray, H. Oetjen, M. Ridolfi, M. Riese, J. Russell, R. Saunders, C. Serio, FORUM: unique far-infrared satellite observations to better understand how Earth radiates energy to space, Bull. Am. Meteorol. Soc. (2020) 1–52.
[4] L. Sgheri, C. Belotti, M. Ben-Yami, G. Bianchini, B. Carnicero Dominguez, U. Cortesi, W. Cossich, S. Del Bianco, G. Di Natale, T. Guardabrazo, D. Lajas, T. Maestri, D. Magurno, H. Oetjen, P. Raspollini, C. Sgattoni, The FORUM end-to-end simulator project: architecture and results, Atmos. Meas. Tech. 15 (3) (2022) 573–604.
[5] W. Zdunkowski, T. Trautmann, A. Bott, Radiation in the Atmosphere: A Course in Theoretical Meteorology, Cambridge University Press, 2007.
[6] W.L. Godson, The evaluation of infra-red radiative fluxes due to atmospheric water vapour, Q. J. R. Meteorol. Soc. 79 (1953) 367–379.
[7] C.D. Rodgers, Inverse methods for atmospheric sounding, WORLD SCIENTIFIC, 2000.
[8] M.K. Transtrum, B.B. Machta, J.P. Sethna, Geometry of nonlinear least squares with applications to sloppy models and optimization., Phys. Rev. E 83 3 Pt 2 (2011) 036701.
[9] I. Gordon, L. Rothman, R. Hargreaves, R. Hashemi, E. Karlovets, F. Skinner, E. Conway, C. Hill, R. Kochanov, Y. Tan, P. Wcisło, A. Finenko, K. Nelson, P. Bernath, M. Birk, V. Boudon, A. Campargue, K. Chance, A. Coustenis, B. Drouin, J. Flaud, R. Gamache, J. Hodges, D. Jacquemart, E. Mlawer, A. Nikitin, V. Perevalov, M. Rotger, J. Tennyson, G. Toon, H. Tran, V. Tyuterev, E. Adkins, A. Baker, A. Barbe, E. Canè, A. Császár, A. Dudaryonok, O. Egorov, A. Fleisher, H. Fleurbaey, A. Foltynowicz, T. Furtenbacher, J. Harrison, J. Hartmann, V. Horneman, X. Huang, T. Karman, J. Karns, S. Kassi, I. Kleiner, V. Kofman, F. Kwabia-Tchana, N. Lavrentieva, T. Lee, D. Long, A. Lukashevskaya, O. Lyulin, V. Makhnev, W. Matt, S. Massie, M. Melosso, S. Mikhailenko, D. Mondelain, H. Müller, O. Naumenko, A. Perrin, O. Polyansky, E. Raddaoui, P. Raston, Z. Reed, M. Rey, C. Richard, R. Tóbiás, I. Sadiek, D. Schwenke, E. Starikova, K. Sung, F. Tamassia, S. Tashkun, J. Vander Auwera, I. Vasilenko, A. Vigasin, G. Villanueva, B. Vispoel, G. Wagner, A. Yachmenev, S. Yurchenko, The HITRAN2020 molecular spectroscopic database, J. Quant. Spectrosc. Radiat. Transfer 277 (2022) 107949.
[10] J. Harries, B. Carli, R. Rizzi, C. Serio, M. Mlynczak, L. Palchetti, T. Maestri, H. Brindley, G. Masiello, The far-infrared earth, Rev. Geophys. 46 (4) (2008).
[11] C. Sgattoni, M. Ridolfi, C. Zugarini, L. Sgheri, Characterization of surface spectral emissivity retrieved from EE9-FORUM simulated measurements, Remote Sens. Earth Syst. Sci. 7 (2024) 15–25.
[12] Z.L. Li, H. Wu, N. Wang, S. Qiu, J.A. Sobrino, Z. Wan, B.H. Tang, G. Yan, Land surface emissivity retrieval from satellite data, Int. J. Remote Sens. 34 (9–10) (2013) 3084–3127.
[13] M. Ben-Yami, H. Oetjen, H. Brindley, W. Cossich, D. Lajas, T. Maestri, D. Magurno, P. Raspollini, L. Sgheri, L. Warwick, Emissivity retrievals with FORUM's end-to-end simulator: challenges and recommendations, Atmos. Meas. Tech. 15 (6) (2022) 1755–1777.
[14] M. Ridolfi, L. Sgheri, Iterative approach to self-adapting and altitude-dependent regularization for atmospheric profile retrievals, Opt. Express 19 (27) (2011) 26696–26709.
[15] L. Sgheri, P. Raspollini, M. Ridolfi, Auto-adaptive tikhonov regularization of water vapor profiles: application to FORUM measurements, Appl. Anal. 101 (10) (2022) 3733–3743.
[16] C.J. Merchant, S. Saux-Picart, J. Waller, Bias correction and covariance parameters for optimal estimation by exploiting matched in-situ references, Remote Sens. Environ. 237 (2020) 111590.
[17] EUMETSAT, IASI level 2: Product guide, 2020, https://www-cdn.eumetsat.int/files/2020-07/IASILevel2_ProductGuide.pdf. (Accessed 06 June 2024).
[18] F.W. Irion, J.M. Blaisdell, E.J. Fetzer, E. Fishbein, A. Goodman, B.H. Kahn, E. Manning, R. Monarrez, M.M. Schreierand, H.T. Thrastarson, Q. Yue, Algorithm theoretical basis document for the Joint Single Footprint Retrieval Algorithm (JoSFRA), Jet Propulsion Laboratory, California Institute of Technology, 2024, https://docserver.gesdisc.eosdis.nasa.gov/public/project/Sounder/JoSFRA_V2_ATBD.pdf. (Accessed 06 June 2024).
[19] J. Susskind, C. Barnet, J. Blaisdell, Determination of atmospheric and surface parameters from simulated AIRS/AMSU/HSB sounding data: Retrieval and cloud clearing methodology, Adv. Space Res. 21 (3) (1998) 369–384, Remote Sensing: Inversion Problems and Natural Hazards.
[20] P. Rosenkranz, Rapid radiative transfer model for AMSU/HSB channels, IEEE Trans. Geosci. Remote Sens. 41 (2) (2003) 362–368.
[21] Y. Han, H.E. Revercomb, M. Cromp, D. Gu, D.G. Johnson, D.L. Mooney, D. Scott, L.L. Strow, G.E. Bingham, L. Borg, Y. Chen, D. DeSlover, M. Esplin, D. Hagan, X. Jin, R.O. Knuteson, H.E. Motteler, J.P. Predina, L. Suwinski, J.K. Taylor, D.C. Tobin, D.A. Tremblay, C. Wang, L. Wang, L. Wang, V.V. Zavyalov, Suomi NPP CrIS measurements, sensor data record algorithm, calibration and validation activities, and record data quality, J. Geophys. Res.: Atmos. 118 (2013) 12,734 – 12,748.
[22] E. Vermote, B. Franch, J. Roger, I. Csiszar, Algorithm theoretical basis document for NOAA NDE VIIRS surface reflectance, 2018, https://www-cdn.eumetsat.int/files/2020-07/IASILevel2_ProductGuide.pdf. (Accessed 06 June 2024).
[23] X. Huang, X. Chen, D.K. Zhou, X. Liu, An observationally based global band-by-band surface emissivity dataset for climate and weather simulations, J. Atmos. Sci. 73 (9) (2016) 3541–3555.
[24] E. Borbas, L. Moy, S. Seemann, R. Knuteson, P. Antonelli, J. Li, H.-L. Huang, I. Trigo, L. Zhou, A global infrared land surface emissivity database and its validation, Res. Gate (2007).
[25] S.W. Seemann, E.E. Borbas, R.O. Knuteson, G.R. Stephenson, H.-L. Huang, Development of a global infrared land surface emissivity database for application to clear sky sounding retrievals from multispectral satellite radiance measurements, J. Appl. Meteorol. Climatol. 47 (1) (2008) 108–123.
[26] NASA JPL, ASTER global emissivity dataset, 100-meter, HDF5, 2014, http://dx.doi.org/10.5067/Community/ASTER_GED/AG100.003, distributed by NASA EOSDIS Land Processes Distributed Active Archive Center, (Accessed 11 August 2023).
[27] G.C. Hulley, S.J. Hook, E. Abbott, N. Malakar, T. Islam, M. Abrams, The ASTER global emissivity dataset (ASTER GED): Mapping earth's emissivity at 100 meter spatial scale, Geophys. Res. Lett. 42 (19) (2015) 7966–7976.
[28] E.E. Borbas, G. Hulley, M. Feltz, R. Knuteson, S. Hook, The combined ASTER MODIS emissivity over land (CAMEL) Part 1: Methodology and high spectral resolution application, Remote Sens. 10 (4) (2018).
[29] M. Feltz, E. Borbas, R. Knuteson, G. Hulley, S. Hook, The combined ASTER MODIS emissivity over land (CAMEL) Part 2: Uncertainty and validation, Remote Sens. 10 (5) (2018).
[30] G. Masiello, C. Serio, S. Venafra, I. DeFeis, E.E. Borbas, Diurnal variation in sahara desert sand emissivity during the dry season from IASI observations, J. Geophys. Res.: Atmos. 119 (3) (2014) 1626–1638.
[31] H. Hersbach, B. Bell, P. Berrisford, S. Hirahara, A. Horányi, J. Muñoz-Sabater, J. Nicolas, C. Peubey, R. Radu, D. Schepers, A. Simmons, C. Soci, S. Abdalla, X. Abellan, G. Balsamo, P. Bechtold, G. Biavati, J. Bidlot, M. Bonavita, G. De Chiara, P. Dahlgren, D. Dee, M. Diamantakis, R. Dragani, J. Flemming, R. Forbes, M. Fuentes, A. Geer, L. Haimberger, S. Healy, R.J. Hogan, E. Hólm, M. Janisková, S. Keeley, P. Laloyaux, P. Lopez, C. Lupu, G. Radnoti, P. de Rosnay, I. Rozum, F. Vamborg, S. Villaume, J.N. Thépaut, The ERA5 global reanalysis, Q. J. R. Meteorol. Soc. 146 (730) (2020) 1999–2049.
[32] Copernicus Atmosphere Monitoring Service (CAMS), CAMS global greenhouse gas reanalysis (EGG4), 2020, https://atmosphere.copernicus.eu/cams-global-greenhouse-gas-reanalysis. (Accessed 23 September 2024).
[33] J.J. Remedios, R.J. Leigh, A.M. Waterfall, D.P. Moore, H. Sembhi, I. Parkes, J. Greenhough, M.P. Chipperfield, D. Hauglustaine, MIPAS reference atmospheres and comparisons to V4.61/V4.62 MIPAS level 2 geophysical data sets, Atmos. Chem. Phys. Discuss. 7 (2007) 9973–10017.

[34] C.D. Peters-Lidard, D.M. Mocko, M. Garcia, J.A. Santanello Jr., M.A. Tischler, M.S. Moran, Y. Wu, Role of precipitation uncertainty in the estimation of hydrologic soil properties using remotely sensed soil moisture in a semiarid environment, Water Resour. Res. 44 (5) (2008).
[35] M. Friedl, D. Sulla-Menashe, MCD12C1 MODIS/Terra+Aqua land cover type yearly L3 global 0.05Deg CMG V006, 2015, NASA EOSDIS Land Processes Distributed Active Archive Center.
[36] National Snow and Ice Data Center, Science of Sea Ice, University of Colorado, Boulder, 2023, https://nsidc.org/learn/parts-cryosphere/sea-ice/science-sea-ice. (Accessed 13 November 2023).
[37] J.W. Salisbury, D.M. D'Aria, Emissivity of terrestrial materials in the 8–14 μm atmospheric window, Remote Sens. Environ. 42 (2) (1992) 83–106.
[38] L. McMillin, M. Goldberg, The use of super channels for high resolution soundings, in: Proceedings of the Ninth International TOVS Conference, Igls, Austria, 1997, pp. 327–330.
[39] M. Matricardi, A principal component based version of the RTTOV fast radiative transfer model, Q. J. R. Meteorol. Soc. 136 (652) (2010) 1823–1835.
[40] C. Clerbaux, A. Boynard, L. Clarisse, M. George, J. Hadji-Lazaro, H. Herbin, D. Hurtmans, M. Pommier, A. Razavi, S. Turquety, C. Wespes, P.F. Coheur, Monitoring of atmospheric composition using the thermal infrared IASI/MetOp sounder, Atmos. Chem. Phys. 9 (16) (2009) 6041–6054.